

A single nanobody neutralizes multiple epochally evolving human noroviruses by modulating capsid plasticity

Received: 22 March 2023

Accepted: 28 September 2023

Published online: 16 October 2023

 Check for updates

Wilhelm Salmen¹, Liya Hu¹, Marina Bok², Natthawan Chaimongkol³, Khalil Ettayebi⁴, Stanislav V. Sosnovtsev³, Kaundal Soni¹, B. Vijayalakshmi Ayyar⁴, Sreejesh Shanker¹, Frederick H. Neill⁴, Banumathi Sankaran⁵, Robert L. Atmar^{4,6}, Mary K. Estes^{4,6}, Kim Y. Green³, Viviana Parreño² & B. V. Venkataram Prasad^{1,4} ✉

Acute gastroenteritis caused by human noroviruses (HuNoVs) is a significant global health and economic burden and is without licensed vaccines or anti-viral drugs. The GII.4 HuNoV causes most epidemics worldwide. This virus undergoes epochal evolution with periodic emergence of variants with new antigenic profiles and altered specificity for histo-blood group antigens (HBGA), the determinants of cell attachment and susceptibility, hampering the development of immunotherapeutics. Here, we show that a llama-derived nanobody M4 neutralizes multiple GII.4 variants with high potency in human intestinal enteroids. The crystal structure of M4 complexed with the protruding domain of the GII.4 capsid protein VP1 revealed a conserved epitope, away from the HBGA binding site, fully accessible only when VP1 transitions to a “raised” conformation in the capsid. Together with dynamic light scattering and electron microscopy of the GII.4 VLPs, our studies suggest a mechanism in which M4 accesses the epitope by altering the conformational dynamics of the capsid and triggering its disassembly to neutralize GII.4 infection.

Human noroviruses (HuNoVs), members of the genus *Norovirus* in the family *Caliciviridae*, are the leading causative agents of epidemic and sporadic acute viral gastroenteritis worldwide^{1,2}. While most immunocompetent patients recover without treatment, norovirus infection can be life-threatening in infants, the elderly, and people with underlying diseases³. It is estimated that HuNoVs cause ~684 million illnesses and ~212,000 deaths annually^{4–7}. The direct health system and societal costs are estimated to be over \$60 billion per year⁸. Despite the substantial societal and economic burdens caused by HuNoVs, no antivirals or norovirus vaccines are available⁷.

Noroviruses (NoVs) are nonenveloped, positive-sense single-stranded RNA viruses with a genome consisting of three open reading frames (ORFs). ORF2 and ORF3 encode the major capsid protein VP1 and the minor structural protein VP2, respectively⁹. The amino acid sequence of VP1 is used to classify NoVs into at least ten genogroups (GI–GX), which are further subdivided into 49 genotypes¹⁰. Among these genogroups, GI, GII, GIV, GVIII, and GIX infect humans, and the viruses in the GII genogroup and genotype 4 (GII.4) are the most predominant. These viruses exhibit preferential accumulations of mutations within VP1 that have indicated the occurrence of genetic drift and selection with each variant descended from chronological

¹Verna and Marrs McLean Department of Biochemistry and Molecular Pharmacology, Baylor College of Medicine, Houston, TX, USA. ²Virology Institute and Technology Innovation, IVIT, CONICET-INTA, Hurlingham, Buenos Aires, Argentina. ³Caliciviruses Section, National Institute of Allergy and Infectious Diseases, National Institutes of Health, Bethesda, MD, USA. ⁴Department of Molecular Virology and Microbiology, Baylor College of Medicine, Houston, TX, USA. ⁵Berkeley Center for Structural Biology, Molecular Biophysics and Integrated Bioimaging, Lawrence Berkeley Laboratory, Berkeley, CA, USA. ⁶Department of Medicine, Baylor College of Medicine, Houston, TX, USA. ✉e-mail: vprasad@bcm.edu

predecessors¹¹. Observed genetic findings and changes in epidemiology indicate population immunity drives the epochal evolution of GII.4 norovirus with the periodic emergence of a variant with new antigenic profiles replacing the previous variant as a means of immune evasion¹¹, similar to H3N2 influenza A virus¹².

Despite the initial obstacles to HuNoV cultivation, there has been remarkable progress in using human intestinal enteroid (HIE) systems for virus replication to study the determinants of infectivity, innate immune responses, and antibody-mediated neutralization^{13–15}. However, there are still challenges in these systems to successfully propagate and obtain the virus in sufficient quantities for structural and biochemical studies, which still rely on virus-like particles (VLPs) produced by the co-expression VP1 and VP2¹⁶. These VLPs are structurally and immunologically similar to authentic virions. While there are some considerable drawbacks to using VLPs, such as the lack of genomic RNA, which may play a role in differentially stabilizing the virus capsid, the use of these VLPs has been invaluable in understanding the structural, immunological, and biological aspects of many strains of HuNoVs¹⁷.

To date, the structures of several caliciviruses have been determined, including feline calicivirus¹⁸, San Miguel sea lion virus¹⁹, murine norovirus (MNV)^{20–22}, and HuNoV VLPs^{23–28} using X-ray crystallography and high-resolution cryo-electron microscopy (cryo-EM). These structural studies have shown that the capsid of calicivirus virions consists of 90 copies of VP1 dimers assembled with a $T=3$ icosahedral symmetry^{28,29}. Each VP1 subunit consists of an internal N-terminal arm (NTA) and two distinct domains, termed shell (S-) and protruding (P-) domain, separated by a flexible hinge²⁹ (see Supplementary Fig. 1). As first observed in MNV^{22,30,31}, recent structural studies^{21,23–25,28} on HuNoV VLPs have shown that VP1 can exist in two distinct conformations, the “resting” conformation in which the P-domain closely interacts with the S-domain, and the “raised” conformation in which the P-domain is rotated and raised above the S-domain, which is driven either by the removal of stabilizing ions, as in the case of GII.4 VLPs²⁸, or with increase in pH, as in case of MNV²¹. The P-domain is further divided into P1 and P2 subdomains, with the distal P2 subdomain involved in recognition of cell attachment factors, which is in the case of GII.4 HuNoV are the histo-blood group antigens (HBGAs) that are also the susceptibility factors^{32,33} (see Supplementary Fig. 1) The HuNoV VLPs have been useful in the biochemical epitope mapping and structural characterization of the human-derived neutralizing and non-neutralizing monoclonal antibodies (mAbs)^{14,34–43}.

In addition to the traditional mAbs, llama-derived single-domain antibodies, also known as ‘nanobodies’, that recognize the HuNoV P-domain have been identified^{38,42,44}. Nanobodies have several advantages over traditional antibodies for their development as immunotherapeutic agents. They are smaller in size (~15 kDa), exhibit higher stability over a wide range of temperatures, and are resistant to protease cleavage^{45–47}. There has also been substantial work done on the development of nanobodies against several other viral agents, such as hepatitis B virus⁴⁸, influenza virus⁴⁹, human immunodeficiency virus⁵⁰, poliovirus⁵¹, rotavirus⁵², and respiratory syncytial virus⁵³. We have previously developed a panel of nanobodies against both prototype GI.1 (Norwalk-1968) and the predominant GII.4 (MD2004) VLPs⁴⁴. Among these nanobodies, we chose M4 as it recognized multiple GII HuNoV strains belonging to genotypes 1, 2, 3, 4, 6, and 7 via ELISA⁴⁴ and inhibited GII.4 VLP binding to HBGA and saliva, suggesting that it has a strong potential for further development as a therapeutic agent against HuNoVs⁴⁴. However, whether M4 can inhibit virus replication and how it recognizes the GII HuNoV has remained unclear.

Here, using HIEs, we show that M4 inhibits replication of GII.4 HuNoVs very effectively. To understand the mechanism of the M4-mediated neutralization, we determined the crystal structure M4 in

complex with GII.4 P-domain. The structure reveals a conserved epitope among GII HuNoVs, which remarkably overlaps with the epitopes of infection- and vaccine-derived human mAbs^{34,54}. Modeling of M4 onto GII.4 capsid structure with VP1 in “resting” and “raised” conformations indicates that M4 binds to the raised VP1 conformation. Along with negative-stain EM these observations suggest that M4 uses a novel neutralization mechanism by restricting the conformational plasticity of the capsid to induce stress and mediate the disassembly of virus particles. Our study provides a molecular basis for the further development of nanobody as a therapeutic agent against HuNoVs.

Results

M4 neutralized multiple strains of GII.4 HuNoVs

To examine the neutralization potential of M4, which showed binding to multiple GII VLPs in previous studies⁴⁴, we infected HIE cultures with 10% stool filtrates containing either GII.3 or different variants of GII.4 HuNoV. M4 effectively neutralized the infection of all the GII.4 HuNoV variants were used in our studies including GII.4 Sydney, GII.4 New Orleans, and GII.4 Den Haag with an IC₅₀ of 53 ng/ml, 56 ng/ml, and 379 ng/ml, respectively (Fig. 1). Interestingly, despite binding to GII.3 VLPs⁴⁴, M4 did not neutralize GII.3 HuNoV infection.

Crystal structure shows molecular interactions between M4 and GII.4 P-domain

To define the epitope recognized by M4, we determined the crystal structure of M4 in complex with the GII.4 Sydney P-domain at a resolution of 2.87 Å (Table 1, Fig. 2a). Two molecules of M4 bind symmetrically to the P-domain dimer with each epitope composed of a buried accessible surface of area (ASA) of 673.7 Å² on subunit A and 224.1 Å² on subunit B. The M4-binding site, on the side of the P-domain dimer closer to the S-domain in the context of the capsid structure, is away from the HBGA-binding site, indicating neutralization by M4 is not by direct blocking of the HBGA (Fig. 2a). A superposition of the structures of GII.4 Sydney P-domain alone and in complex with M4 and in complex with H-type HBGA showed that M4 binding does not result in any significant conformational changes in the P-domain, with a root mean square deviation of 0.68 Å between matching C α atoms, and the HBGA-binding site is not affected (Fig. 2b).

The crystal structure of M4 in complex with GII.4 P-domain reveals the molecular details of the interactions. M4 binding near the P-domain dimeric interface involves residues from each of the subunits through a network of hydrogen-bonding and hydrophobic interactions. The majority of these interactions on each side of the dimer involve one of the subunits with residues from both P1 and P2 subdomains (Supplementary Fig. 1) participating in the interactions (Fig. 2c–e). The paratope in M4 consists of eleven residues from all three complementarity-determining regions (CDRs), with residues R99, R100, D101, L102, R105, F106 in CDR3 contributing to most of the interactions with the P-domain (Fig. 2c, d). For instance, R100 in the CDR3 of M4 hydrogen bonds with L272, G274, and T276 in the P-domain subunit, R99 and R105 in the CDR3 hydrogen bond with the side chains D269 in subunit A and E236 in subunit B of the P-domain dimer, respectively (Fig. 2e). Residues D101, L102, and F106 in CDR3 make van der Waals contacts with residues L232, T233, G270, L273, Y462, P480, and Y514 of the P-domain (Fig. 2e). In addition to CDR3, residues I31 in CDR1 and T52 and G54 in CDR3 are in contact with residues K493, H417, and E316 of the P-domain (Fig. 2e). Furthermore, non-CDR residues Q1 and S27 of M4 also interact with A465 and K493 of the P-domain via hydrogen-bonding and hydrophobic interactions (Fig. 2d).

M4-binding site is highly conserved among GII HuNoVs

The alignment of the P-domain amino acid sequences of 26 GII genotypes (Fig. 3) shows that the identified M4-binding site in our crystallographic structure is highly conserved (72% to 94% identity),

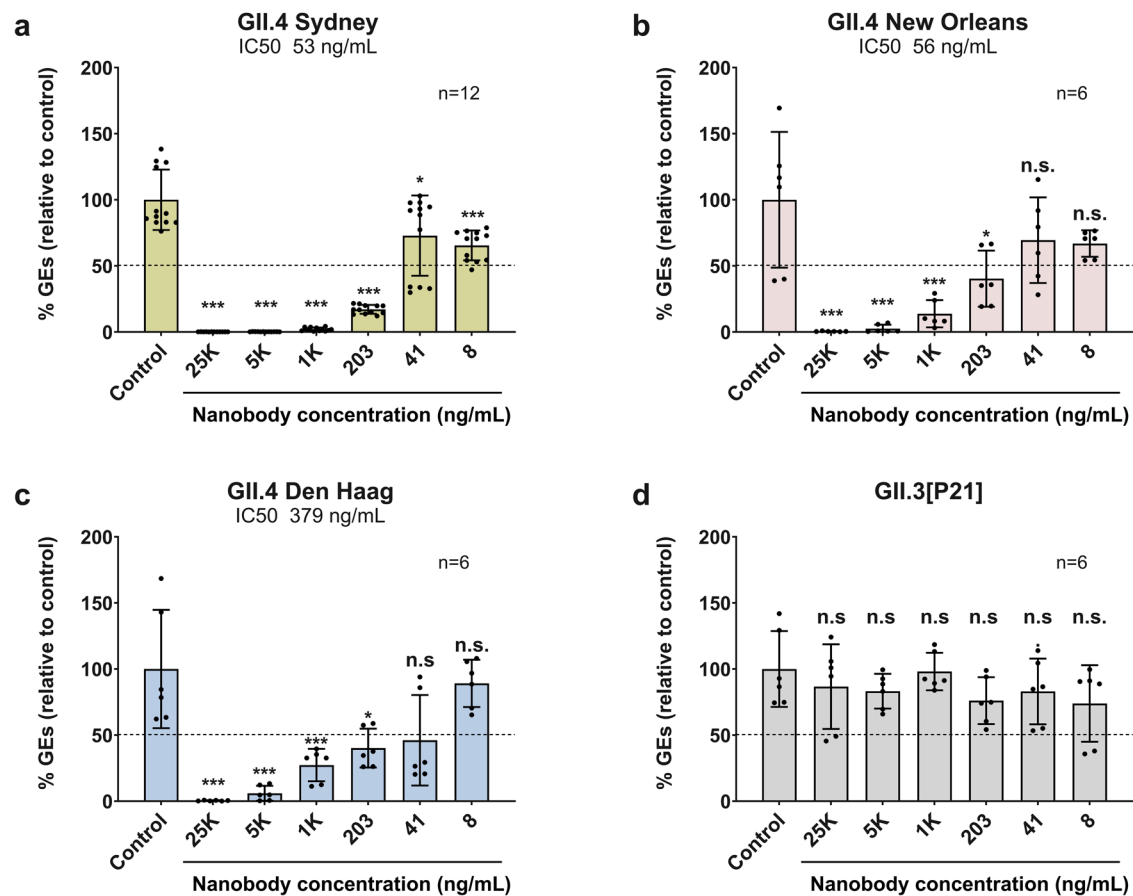


Fig. 1 | M4 nanobody neutralizes GII.4 variants, but not GII.3, in human intestinal enteroid system. Serial dilutions of M4, in differentiation medium supplemented with 500 μ M GCDCA, were preincubated with equal volume of the same medium containing 100 TCID₅₀ of HuNoV for 1 hr at 37 °C. The M4/virus mixtures were inoculated in differentiated J4^{FUT2} HIE monolayers. Viral replication was measured by RT-qPCR after 24 hpi. Percent reduction in viral genome equivalents (GEs) relative to the medium control (100%) was determined. The

dotted line represents 50% neutralization. Error bars denote standard deviation and data bars represent the mean of the data collected from the specified number of wells (six wells for **b–d**, and 12 replicates for **a**). Significance relative to the control was determined using two-tailed Student's *t* test. Exact *p* values from left to right: **a** ****p* = 3.9E-13, 4.0E-13, 5.9E-13, 1.9E-11, 1.1E-4, **p* = 0.02; **b** ****p* = 7.8E-4, 9.2E-4, 2.4E-3, **p* = 0.02; **c** ****p* = 2.8E-4, 4.6E-4, 3.3E-3, **p* = 0.01; **d** all differences are n.s., not significant.

consistent with our previous finding that the M4 binds to multiple GII VLPs⁴⁴. Interestingly, 72% conservation of the epitope in the GII.3 P-domain is on the lower side with five residue changes including V271E, L273M, E316D, H417N, and A465S. The epitope region shows only 44% conservation with the VP1 sequence of GI.1 Norwalk virus, which is consistent with our previous result showing that M4 does not bind to Norwalk VP1.

M4 binds to the GII.4 VLP in the “raised” conformation

Recent X-ray crystallographic and cryo-EM studies of GII.4 VLP shows that VP1 can exist in “resting” and “raised” conformations²⁸. To investigate the binding of M4 to the VP1 dimers in the context of the GII.4 capsid structure, we superimposed the M4-GII.4 P-domain complex onto the GII.4 VLP structure in the “resting” (Fig. 4a–d) and “raised” (Fig. 4e–h) states. The structural modeling shows that the M4-epitope is occluded in the “resting” form, and M4 clashes with the neighboring VP1 subunits, suggesting that M4 is unlikely to bind to the P-domain of VP1 in the “resting” state (Fig. 4b). In contrast, in the “raised” *T*=3 state, when the P-domain is raised above the shell domain, the epitope becomes accessible for M4 binding (Fig. 4f). The modeling further suggests that the binding of M4 to the “raised” P-domain would prevent it from rotating and descending back onto the S-domain to the more stable “resting” conformation thereby inducing stress on the stability of the capsid leading to particle disassembly (Fig. 4i).

M4 induces particle disassembly of GII.4 and GII.3 VLPs with different kinetics

To test the hypothesis that M4 binding may affect particle stability leading to disassembly, we performed negative-stain EM, dynamic light scattering (DLS), and sedimentation velocity-analytical ultracentrifugation (SV-AUC) experiments with GII.4 VLPs treated with and without M4 in PBS. Negative-stain EM data suggest that incubation of M4 with GII.4 VLPs leads to particle disintegration, resulting in smaller structures such as *T*=1 particles and capsid fragments (Fig. 4j). Because M4 did not neutralize GII.3 HuNoV in HIEs, we examined whether M4 has a similar effect on GII.3 VLPs using the same experimental procedure. This EM analysis suggested that M4 has a similar effect on GII.3 VLPs (Fig. 4j). Consistent with EM analysis, the DLS data for GII.4 and GII.3 VLPs treated with M4 indicate a significant reduction in the distribution of particle diameters which also likely involves capsid fragments (Supplementary Fig. 2). In the case of GI.1 VLPs, used as a negative control, as the M4 epitope is not conserved in GI.1 (Supplementary Fig. 2C), the diameters remained the same following incubation with M4. To further analyze the capsid disassembly more quantitatively, we performed SV-AUC, of GII.4 and GII.3 VLPs (Supplementary Fig. 3) before and after incubating with M4. When GII.4 and GII.3 VLPs were treated with M4, we observed clear shifts in sedimentation coefficients that indicated a substantial reduction in the molecular weights of the particle fragments. In the case of GII.4 VLPs, we observed a slightly heterogeneous population

Table 1 | Summary of X-ray crystallography data collection and refinement statistics

PDB ID	8GOW
Wavelength (Å)	0.99994
Resolution range (Å)	47.55–2.87 (2.97–2.87)
Space group	P 1 2 ₁ 1
Unit cell	
a, b, c (Å)	103.5, 90.7, 107.2
α, β, γ (°)	90, 113.3, 90
Unique reflections	41401 (4078)
Multiplicity	2.0 (2.0)
Completeness (%)	98.66 (98.26)
Mean I/sigma(I)	5.41/1.95
Wilson B-factor (Å ²)	31.33
R-merge (%)	9.11 (33.4)
R-work (%)	25.05(33.53)
R-free (%)	29.39(38.28)
Number of non-hydrogen atoms	12,812
Macromolecules	12810
Ligands	0
Solvent	2
Protein residues	1653
R.M.S. deviations	
Bond lengths (Å)	0.002
Bond angles (°)	0.56
Ramachandran	
Favored (%)	97.16
Allowed (%)	2.84
Disallowed (%)	0
Average B-factor (Å ²)	34.01
Macromolecules	34.01
Solvent	29.08

Statistics for the highest-resolution shell are shown in parentheses.

of VLPs in the untreated sample that is consistent with molecular weights of capsids with $T=1$ (black peak I), $T=3$ (black peak II), and $T=4$ (black peak III) symmetries (Supplementary Fig. 3A). However, despite showing heterogeneity, when GII.4 VLPs were treated with M4 we observed a significant reduction in percent population of $T=3$ VLPs (red peak IV), complete loss of $T=4$ fraction, and the emergence of smaller fractions (red peaks I, II, III), clearly indicative of particle disintegration (Supplementary Fig. 3A). For the case of GII.3 VLPs, we observed complete disappearance of peaks corresponding to molecular weights consistent with $T=3$ VLPs (black peak IV) and the emergence of peaks with lower molecular weights (red peaks I, II, III) (Supplementary Fig. 3B). Similar experiment with GI.1 VLP treated with M4, used as a negative control, did not show any change in sedimentation coefficients (Supplementary Fig. 3C). Together, these experiments clearly demonstrate that M4 triggers disassembly of both GII.4 and GII.3 VLPs.

Further, to examine if there are differences in the kinetics of M4 binding to the GII.4 and GII.3 P-domains, we used bilayer interferometry (BLI). These experiments show that M4 binds to both the GII.4 and GII.3 P-domains with strong binding affinity of K_D of $<1 \times 10^{-12}$ M and K_D of $4.8\text{--}7.8 \times 10^{-10}$ M, respectively (Supplementary Fig. 4), despite 72% conservation in the M4 epitope. The modest differences in the binding affinities between GII.4 and GII.3 are consistent with the observation that there are only two non-conserved mutations (V271E and A465S) in the M4-binding regions of these

viruses. Despite exhibiting similar binding on rates, the off rates of M4 binding to GII.4 and GII.3 VLPs were significantly different with $K_{dis} = <1 \times 10^{-7}$ per second for GII.4 and $K_{dis} = 1.68\text{--}1.90 \times 10^{-3}$ per second for GII.3 (Supplementary Fig. 4). This difference suggests that GII.3 VLP disassembly has a slower kinetics compared to that of GII.4 VLPs, and further the kinetics of particle disassembly depends upon the threshold of stably bound M4 required to trigger the disassembly.

M4 inhibits GII.4-induced endocytosis on HIEs

To test if M4 affects uptake and entry of GII.4 norovirus, we performed endocytosis assays to measure the induction of endocytosis by VLPs in the presence of M4. The effect of M4 nanobody on GII.4-induced endocytosis was confirmed by monitoring uptake of the dye FMI-43FX using epifluorescence microscopy (Supplementary Fig. 5). FMI-43FX is an endocytosis tracking dye that labels extracellular membranes and fluorescent puncta are observed following endocytosis, indicating endocytic trafficking¹⁷. GII.4 VLP-induced endocytosis (represented by the number of fluorescent puncta) is reduced in the presence of M4 nanobody demonstrating that binding of M4 to GII.4 VLP blocks its entry into the HIEs.

Discussion

The enormous genetic and antigenic diversity across circulating strains of HuNoV makes it challenging to identify broadly cross-reactive and neutralizing antibodies for the development of immunotherapeutic agents. In the case of GII.4 HuNoV, which accounts for most episodic events worldwide, this is further exacerbated by the periodic emergence of new variants with altered HBGA specificity, allowing these variants to escape herd immunity¹¹. In this study, from a panel of llama-derived norovirus-specific nanobodies, we discovered that nanobody M4 neutralizes multiple GII.4 variants with high potency in HIEs potentially using a novel mechanism by targeting a conserved region in the P-domain that is distant from the HBGA-binding site.

To date, there have been several crystal structures of antibodies in complex with the P-domain of GI and GII HuNoV VP1, which show varied antibody recognition patterns. The first pattern is the binding of a human-derived antibody to the P-domain of GI HuNoV at a site that overlaps with the HBGA-binding site indicating that the neutralization mechanism of such antibodies is by directly blocking cell attachment³⁶. In the case of GII HuNoVs in general and GII.4 variants in particular, such antibodies that directly block HBGA-binding are unlikely to be broadly cross-reactive, as the epitopes surrounding the HBGA-binding site exhibit sequence variability^{55–57}. The second pattern is antibody binding to the sides of the P-domain dimer away from the HBGA-binding site but still blocking cell attachment to neutralize infection by mediating particle aggregation/cross-linking, as shown with the GII.4-specific antibodies such as human-derived NORO-320 and A1431 (Fig. 5a)^{14,34}. Our studies show that the neutralization mechanism of M4 is distinct from either of these cases. As M4 binds away from the HBGA-binding site, it cannot directly block HBGA binding, and as the binding is monovalent, it cannot mediate cross-linking-specific aggregation blocking cell attachment (Fig. 5d). Surprisingly, we observed that M4 shares a considerable overlap with the non-neutralizing mAb A1227 which suggests that the larger size of A1227 results in increased steric clash and reduced binding to intact virions compared to M4 (Fig. 5b)³⁴.

When we model the M4 binding onto the recently published crystal structure of the GII.4 VLP²⁸, it is apparent that there is a significant steric clash between M4 and the neighboring VP1 dimers. It has recently been shown that GII.4 VP1 can be conformationally dynamic by adopting “resting” and “raised” conformations in the $T=3$ capsid²⁸. When the capsid adopts the stable “resting” conformation, M4 binding is sterically prohibitive (Fig. 4a–d). However, these steric clashes near

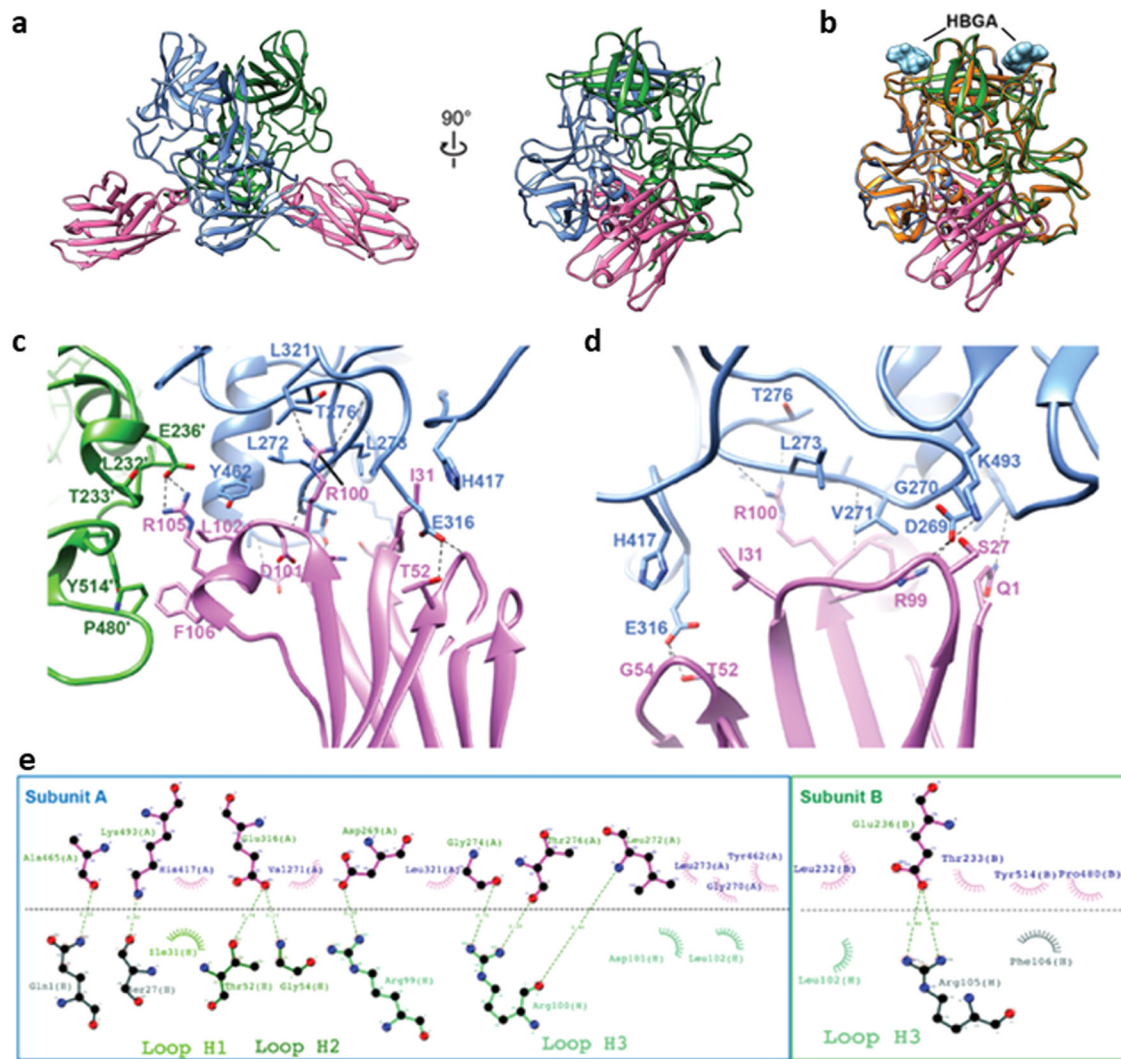


Fig. 2 | Nanobody M4 in complex with GII.4 Sydney/2012 P-domain. **a** X-ray crystal structure of the M4-GII.4 P-domain complex. The two subunits of the P-domain dimer are colored blue and green. Nanobody M4 is shown in pink. **b** Superposition of M4-GII.4 P-domain complex with HBGA-GII.4 P-domain structure (orange, PDB ID: 5J35). The glycan fucosyllactose (2'-FL) is shown as cyan spheres to indicate the HBGA-binding sites for reference. **c, d** Close-up views of the

interactions of M4 with two subunits of P-domain dimer. The subunits A and B of the P-domain dimer are colored in blue and green, respectively. The side chains of M4 and P-domain are shown as stick representations. The hydrogen bonds are shown as black dashed lines. **e** Antibody plot analysis using the program LigPlot+v.2.2.5. Green dashed lines indicate the hydrogen bonds, and short spokes radiating from each atom or residue represent the hydrophobic contacts.

the M4-binding site are lost when the P-domain breaks the stabilizing hydrogen bonds at the S-P-domain interface, rotates, and elevates above the shell domain transiting to the “raised” conformation (Fig. 4e–h). The kinetic equilibrium between the two states can be altered by variations in ionic strength or pH variations^{21,28}, allowing some VP1 subunits in the capsid to adopt “raised” conformation, thereby allowing access for M4 binding. M4 bound to the “raised” P-domain can act like a “lock” to prevent the P-domain from rotating back to rest on S-domain thereby restricting plasticity of the capsid and the particle becomes less stable as it loses several hydrogen-bonding contacts between the P and S domains (Fig. 4f). Considering that the binding affinity for M4 is high, M4 binding to several VP1 subunits can progressively destabilize the entire capsid. Indeed, when VLPs are treated with M4 and imaged using negative-stain EM, we observed particle disassembly into small debris (Fig. 4j). It is to be noted that M4-induced disassembly occurs even without the removal of bound cation, which has been shown necessary to trigger the transition from the resting to the raised state in the case of GII.4 VLP²⁸ and without changes in pH, which also may be a factor in triggering the conformational transition²¹. These results indicate M4 can readily alter

the equilibrium between the resting and rising conformations and bind to its epitope regardless of external factors.

Further, recent work has shown that GII.4 VLPs and virions, but not P-domain alone, induce endosomal acidification to initiate endocytosis and uptake of the virus¹⁷. We performed similar endocytosis experiments with GII.4 VLPs in the presence of M4 and observed the endocytic uptake is significantly diminished, consistent with capsid disassembly by M4 as a possible mechanism of neutralization (Supplementary Fig. 5). Like M4, nanobody Nano-85 and monoclonal antibody 5B18, recognize an epitope near the S-P-domain occluded in the intact virion with VP1 adopting a resting conformation and disassemble the GII.4 VLPs (Fig. 5c)^{35,38}. Although there have been no neutralization assays performed, Nano-85 and monoclonal antibody 5B18 are speculated to facilitate neutralization by disassembling the particles.

A remarkable observation from our studies is that M4 can neutralize multiple variants of GII.4 HuNoVs with potency significantly higher than other neutralizing antibodies reported to date. When compared to neutralization by NORO-320 mAb and Fab with IC₅₀ values of 11,690 ng/ml (33.4 nM) and 2950 ng/ml (59 nM)



Fig. 3 | Amino acid sequence alignment of the protruding domain.

VP1 sequences of 26 GII genotypes and one GI.1 genotype are aligned using ClustalW and visualized by Jalview. The M4-binding residues are colored using ClustalX shading scheme to highlight amino acid conservation.

respectively¹⁴, M4 neutralizes GII.4 Sydney HuNoV with an IC_{50} of 53 ng/ml (4 nM). The neutralization efficiency of M4 is also comparable to 10E9 mAb (Fab fraction), which showed a GII.4 neutralization by blocking HBGA binding with an IC_{50} of 97 ng/ml (2 nM) in HIE⁴³. The better efficiency of M4 compared to NORO-320 may be due to its smaller size to minimize steric clash and higher affinity of binding to more readily engage its epitope to trigger disassembly.

An intriguing observation from our studies is that although M4 binds and disassembles GII.3 VLPs, similar to GII.4 VLPs (Fig. 4j), M4 only neutralizes GII.4 HuNoV and not GII.3 HuNoV (Fig. 1). This observation suggests that M4 cannot readily access the epitope in the GII.3 virions, perhaps because of significantly slower transition kinetics between the “resting” and “raising” states in the GII.3 virion compared to that in the GII.3 or GII.4 VLPs, and also to the GII.4 virion. Although the structures of $T = 3$ GII.3²¹ and GII.4 VLPs²⁸ are highly similar in their resting conformations, GII.3 VLPs appear to exhibit slower kinetics of transition between the resting and raised conformations. With changes in pH or ion chelation, only 16% of the total GII.3 VLPs transit to the raised P-domain conformation and the elevation of the P-domain in the raised state is -4 \AA lower than the observed height for murine norovirus²¹. In our infectivity assays, M4 fails to neutralize GII.3 even after incubating the virus with M4 for an hour. In contrast, M4 disassembles both GII.4 and GII.3 VLPs within 30 min of adding M4, suggesting that the capsid structure in the GII.3 virion is intrinsically more stable than that in the VLPs or in the GII.4 virion. It is plausible that the genome along with VP2 in the GII.3 virion, contribute differentially to the increased stability of the capsid. Our studies thus underscore, despite a conserved epitope, how the capsid stability and

plasticity variations between genotypes may influence the mechanism of neutralization.

In summary, our studies presented here provide insight into a plausible novel mechanism of a nanobody that neutralizes multiple GII.4 NoV variants with high potency by targeting a highly conserved epitope that is vulnerable to inherent conformational dynamics of the viral capsid. Given the advantages associated with nanobodies, these studies could be helpful in further optimization of nanobody scaffolds as efficient immunotherapeutic agents for periodically evolving GII.4, and possibly other GII HuNoVs.

Methods

Virus neutralization assay

Human jejunal intestinal enteroids (J4^{FUT2} HIEs⁵⁸) were plated and differentiated as HIE monolayers in collagen IV-coated 96-well plates in commercial Intesticult human organoid growth medium (StemCell Technologies, Cat#06010) as previously described⁵⁹. Separately, 100 TCID₅₀ of GII.4 (Sydney 2012), GII.4 (Den Haag), GII.4 (New Orleans), and GII.3 (TCH04-577) stool filtrates were preincubated, in Intesticult differentiation medium supplemented with 500 μM of bile acid glycochenodeoxycholic acid (GCDC), with different concentrations of M4 nanobody for 1 hr at 37 °C. Virus-nanobody mixtures were then added to HIE monolayers and incubated at 37 °C. After 1 hr incubation, the inoculum was removed, and monolayers were washed twice with CMGF [-] medium to remove unbound virus. Intesticult differentiation medium (100 μl containing 500 μM GCDC) was then added to each well, and the cultures were incubated at 37 °C for 24 h. Neutralization in each case was evaluated in two independent assays for each genogroup/variant and samples were run in triplicate in each assay.

Total RNA was isolated from each infected well using the King-Fisher Flex purification system in conjunction with the MagMAX-96 viral RNA isolation kit. RNA extracted at 1 hpi served as the reference point to assess the remaining quantity of viral material associated with cells after washing the infected cultures. For viral quantification, reverse transcriptase quantitative PCR (RT-qPCR) was performed with the QNIF2d/COG2R/QNIF5 primer pair and probe. The reaction was conducted using the qScript XLT One-Step RT-qPCR ToughMix reagent with ROX reference dye (Quanta Biosciences). Amplification was performed on an Applied Biosystems StepOnePlus thermocycler using the following cycling conditions: 50 °C (15 min) and 95 °C (5 min), followed by 40 cycles of 95 °C (15 sec) and 60 °C (35 sec). A standard curve based on a recombinant HuNoV GII.4 RNA transcript was established to quantify viral genome equivalents (GEs) in RNA samples. Viral replication was determined by RNA levels quantified from samples extracted at 24 hpi. Percent reduction in GEs relative to medium (100%) was determined from a total of 6 or 12 readings, comprising biological replicates and technical duplicates to ensure reliability, rigor, and robustness in our data analysis.

Expression and purification of HuNoV VLPs

The VP1 and VP2 of GII.3 (Houston/TCH04-577/USA, AB365435) and GII.4 (Sydney/2012/AUS, JX459908) noroviruses were expressed in the baculovirus system as described previously^{16,60}. Briefly, infected Sf9 cells were grown for 10 days, and the cell suspension was pelleted by centrifugation at $22,100 \times g$ for 30 min. The resulting supernatant was overlaid on a 30% sucrose cushion and VLPs were pelleted by centrifuging at $120,000 \times g$ for 3 h at 4 °C. The pellet was suspended by adding 200 μl of PBS per tube and incubating at 4 °C overnight. Suspended VLPs were then pooled and diluted with PBS containing cesium chloride (1.14 mg/ml) to a final concentration of 0.38 mg/ml cesium chloride. The sample was then centrifuged at $150,000 \times g$ for 18 h at 4 °C. The VLP-containing white band was collected by micropipette and then was dialyzed overnight at 4 °C in PBS pH 6.0. The dialyzed VLPs were then further purified using a Sephacryl S500 size

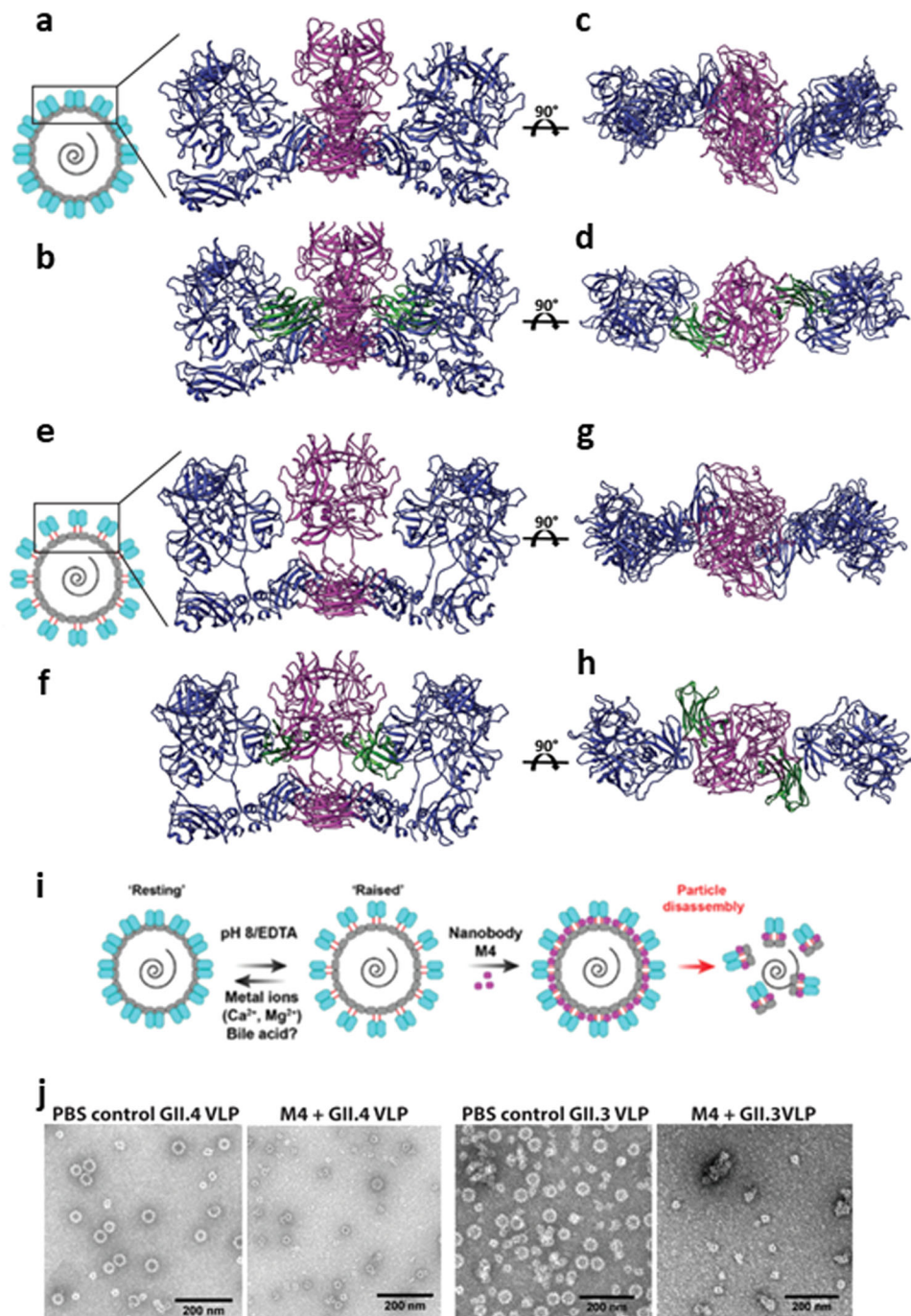


Fig. 4 | Modeling of M4 bound on GII.4 capsid in the “resting” and “raised” states. **a–d** Top view and side view of superimposition of M4-GII.4 P-domain complex onto the AB dimer of HOV VLP cryo-EM structure (PDB ID:7MRY) in “resting” state. **e–h** Top and side view of M4-GII.4 P-domain complex superimposed on the AB dimer of the VLP in the “raised” state, which was modeled in 8.0 Å GII.4c cryo-EM map in $T = 3$ symmetry (EMD-10756). The VPI subunits are

colored (M4 bound dimer, magenta; neighboring dimer, blue). Nanobody M4 is shown in green. **i** Schematic of M4 neutralization mechanism. Cartoon representation of the capsid (designed using Adobe Illustrator) in the resting (as in **a**) and the raised state (as in **e**) shown with P-domain dimers in blue, S domain in green, and linker region in red. **j** Negative-stain EM analysis of GII.4 and GII.3 VLPs in the presence or absence of M4.

exclusion chromatography column. Purified fractions were pooled and stored at 4 °C.

Expression and purification of P-domain and M4

Each of GII.3 (TCH04-577) and GII.4 Sydney 2012 P-domain sequence was cloned into the expression vector pMal-C2E (New England BioLabs). The recombinant P-domain was expressed with an N-terminal His₆-maltose-binding protein (MBP) tag, and a tobacco etch virus (TEV) cleavage site between the MBP and P-domain in *E. coli* BL21(DE3)

and purified using His-Trap (GE Healthcare). The His-MBP tag was then removed using TEV protease and separated from the P-domain by purifying it once again using His-Trap (GE Healthcare), MBPTrap (GE Healthcare) affinity columns, and size exclusion chromatography as previously described⁶¹. The purified P-domain was concentrated and stored in a buffer containing 20 mM Tris-HCl (pH 7.2), 150 mM NaCl, and 2.5 mM MgCl₂. The recombinant M4 was expressed in *E. coli* WK6 strain. The periplasmic proteins were extracted by osmotic shock using Tris/EDTA/Sucrose (TES) buffer, and His-tagged M4 was purified

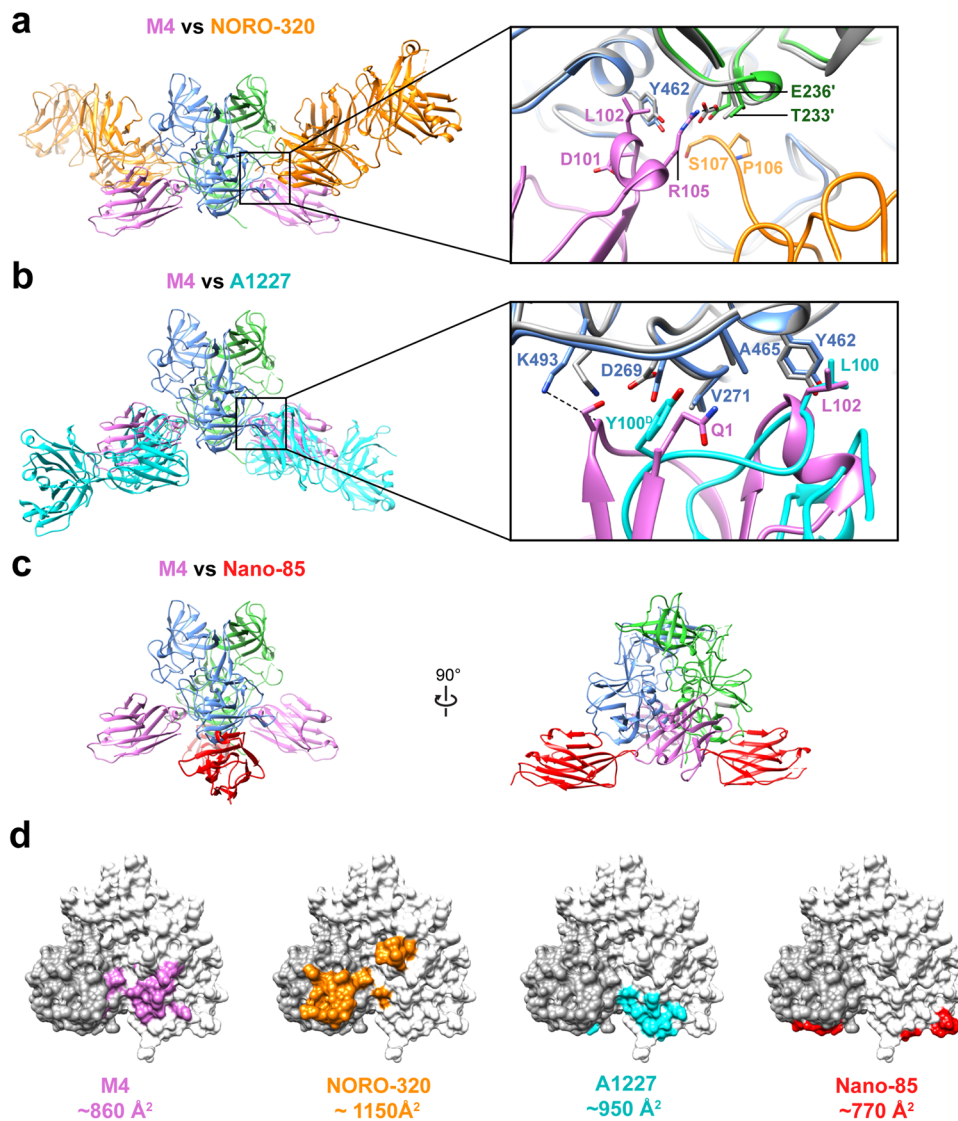


Fig. 5 | Comparison of M4-GII.4 P-domain complex with representative GII.4-mAb or GII.4-nanobody complexes. **a–c** Superimposition of the structure GII.4 P-domain in complex with M4 (pink, PDB ID: 8GOW), NORO-320 Fab (orange, PDB ID: 7JIE), A1227 Fab (cyan, PDB ID: 6N81), or nanobody Nano-85 (red, PDB ID: 4X7D). The subunits A or B of the P-domain dimer are colored in blue and green,

respectively. The insets in (a) and (b) show the close-up view of the epitopes on the P-domain, with key side chains shown in the stick model and labeled. **d** The P-domain dimers are shown with white and dark gray surface representation to define each subunit, with the buried surface on P-domain colored as the corresponding nanobody or Fab.

from the periplasmic extract using a High-Trap HP Ni-chelating column (GE Healthcare, US).

Crystallization of GII.4 P-domain and M4

Purified GII.4 P-domain and M4 were mixed with a 1:1.5 molar ratio and incubated for 1 h at 4 °C. The mixture was passed through an S200pg 16/60 gel filtration column, and the peak corresponding to the complex was collected. The size of the complex and the presence of both proteins were validated on an SDS-PAGE gel. The peak fractions were then pooled and concentrated to 10 mg/ml for crystallization trials. Crystallization screening using a hanging-drop vapor diffusion method at 20 °C was set up using a Mosquito nanoliter handling system (TTP LabTech) with commercially available crystal screens, and crystals were visualized using a Rock Imager (Formulatrix). The M4-GII.4 P-domain complex was crystallized in a buffer containing 2% v/v Tacsimate pH 4.0, 0.1 M Sodium acetate trihydrate pH 4.6, 16% w/v Polyethylene glycol 3350 (Hampton Research).

Data collection and structure determination

Diffraction data were collected on beamline 8.2.2 at Advanced Light Source (Berkeley, CA) and processed using HKL2000⁶². The previously published GII.4 Sydney P-domain structure (PDB ID 7JIE) and the nanobody (PDB ID 5KW9) coordinates were used as the search models by molecular replacement using program PHASER⁶³. Iterative refinement cycles and further model building were carried out using PHENIX⁶⁴ and COOT⁶⁵. Data refinement and statistics are given in Table 1. The interactions between P-domain and the M4 were analyzed using LigPlot+ v.2.2.5⁶⁶. Figures were prepared using Chimera⁶⁷.

Negative-stain EM

GII.4 Sydney VLPs were diluted to a working concentration of 0.50 mg/ml in PBS pH 6.0. VLP was then mixed with PBS or M4 nanobody for a final concentration of 0.25 mg/ml (19.5 μM) of M4 and 0.25 mg/ml (4.23 μM) of VLP. Following the preparation of the mix, each condition was incubated for 30 min at room temperature. A 3 μL aliquot of each sample mixture was applied onto a glow-

discharged 200-mesh 2/2 Quantifoil holey carbon grid containing an 8 nm layer of carbon and incubated for 3 min. Grids were then blotted, washed with Milli-Q H₂O, and then 2% uranyl acetate was applied to the grids for 1 min. Finished grids were stored in a dehumidifier at room temperature. Images were collected at 120 kV on a JEM-1230 EM at a ×25,000 magnification.

Biolayer Interferometry

Biotinylation of the GII.3 and GII.4 P-domains was carried out using EZ-Link NHC-LC-LC-biotin (catalog no. 21343; Thermo Scientific) following the manufacturer's instructions. The P-domain was loaded onto streptavidin biosensors at a concentration of 0.625 µg/ml in the BLI running buffer (20 mM HEPES buffer, 150 mM NaCl, 0.005% surfactant P20, 2 mg/ml bovine serum albumin, pH 7.8) for 300 s, resulting in capture levels of 0.8–1.5 nm within a row of eight tips. M4 was diluted in BLI running buffer to a final concentration of 20 nM and incubated on ice overnight. M4:P-domain association and dissociation curves were obtained through twofold serial dilutions of M4 (20, 10, 5, 2.5, 1.25, 0.625, 0.3125 nM) plus buffer blanks at 30 °C using the Octet acquisition software. BLI studies were carried out using an Octet RED96 instrument (FortéBio).

Dynamic light scattering

The hydrodynamic diameters of GII.4 Sydney and GII.3 TCH-577 VLPs in the absence or presence of M4 at pH 6.0 were measured using DLS on a ZetaSizer Nano instrument (Malvern Instruments, U.K.). VLPs were diluted to a final concentration of 200 nM and M4 was diluted to 800 nM in phosphate-buffered saline (molar ratio 1:4 VPI:M4). Upon addition of M4, samples were incubated on ice for 30 min before measurements were taken. Three × 12 measurement runs were performed with standard settings (Refractive Index 1.335, viscosity 0.9, temperature 25 °C).

Sedimentation velocity-analytical ultracentrifugation

The SV-AUC experiments with VLPs of GI.1 Norwalk, GII.4 Sydney, and GII.3 TCH-577, both alone and in complex with M4, were performed using Beckman-Coulter XL-A analytical ultracentrifuge with a TiAn60 four-hole rotor and two-channel Epon centerpieces (12 mm). VLPs in complex with M4 were prepared at a molar ratio of 1:4 with working concentrations of 1 µM VPI and 4 µM M4, in PBS at pH 6.0, and incubated at 37 °C for 1 h. GI.1 VLPs treated with M4 nanobody were used as negative control. Absorbance scans were recorded at 280 nm at every 1 min interval at 1500 rpm at 4 °C. Continuous distribution c(s) model was used to fit multiple scans at regular intervals with SEDFIT^{68,69}. The solvent density (ρ) and viscosity (η) were calculated from the chemical composition of different proteins by SEDNTERP⁶⁹.

Endocytosis assay

Endocytosis measurements were carried out using FMI-43FX (ThermoFisher Scientific) as described previously¹⁷. Briefly, HIE monolayers were treated with 10 µg/ml of FMI-43FX for 10 min at 37 °C with either VLP alone or VLP preincubated with M4 for 1 h at 37 °C. Monolayers were washed with prechilled PBS and fixed in 4% PFA for 20 min. followed by nuclei staining with 300 nM DAPI for 5 min at room temperature. Endocytic trafficking was measured by the presence of fluorescent puncta which were observed by epifluorescence microscopy using Olympus cellSens Standard Version 2.3 software. Quantitation of the number of fluorescent puncta was done using J-image. Every experiment was repeated at least three times with 4 images analyzed per condition in each experiment.

Statistics and reproducibility

Each experiment was repeated independently at least twice with similar results and representative data were shown.

Reporting summary

Further information on research design is available in the Nature Portfolio Reporting Summary linked to this article.

Data availability

Atomic coordinates and structure factors for the crystal structure of M4 in complex with GII.4 P-domain have been deposited in the Protein Data Bank under the accession code [8GOW](https://doi.org/10.1038/s41467-023-42146-0). The authors declare that all other data supporting the findings of this study are available within the paper and its supplementary information files. Source data are provided with this paper.

References

- Ahmed, S. M. et al. Global prevalence of norovirus in cases of gastroenteritis: a systematic review and meta-analysis. *Lancet Infect. Dis.* **14**, 725–730 (2014).
- Pires, S. M. et al. Aetiology-specific estimates of the global and regional incidence and mortality of diarrhoeal diseases commonly transmitted through food. *PLoS One* **10**, e0142927 (2015).
- Patel, M. M., Hall, A. J., Vinje, J. & Parashar, U. D. Noroviruses: a comprehensive review. *J. Clin. Virol.* **44**, 1–8 (2009).
- Mattison, C. P., Cardemil, C. V. & Hall, A. J. Progress on norovirus vaccine research: public health considerations and future directions. *Expert Rev. Vaccines* **17**, 773–784 (2018).
- Kirk, M. D. et al. World health organization estimates of the global and regional disease burden of 22 foodborne bacterial, protozoal, and viral diseases, 2010: a data synthesis. *PLoS Med.* **12**, e1001921 (2015).
- Wang, H. et al. Global, regional, and national life expectancy, all-cause mortality, and cause-specific mortality for 249 causes of death, 1980–2015: a systematic analysis for the Global Burden of Disease Study 2015. *Lancet* **388**, 1459–1544 (2016).
- Atmar, R. L., Ramani, S. & Estes, M. K. Human noroviruses: recent advances in a 50-year history. *Curr. Opin. Infect. Dis.* **31**, 422–432 (2018).
- Bartsch, S. M., Lopman, B. A., Ozawa, S., Hall, A. J. & Lee, B. Y. Global economic burden of norovirus gastroenteritis. *PLoS One* **11**, e0151219 (2016).
- Vongpunsawad, S., Venkataram Prasad, B. V. & Estes, M. K. Norwalk virus minor capsid protein VP2 associates within the VP1 shell domain. *J. Virol.* **87**, 4818–4825 (2013).
- Chhabra, P. et al. Updated classification of norovirus genogroups and genotypes. *J. Gen. Virol.* **100**, 1393–1406 (2019).
- Siebenga, J. J. et al. Epochal evolution of GII.4 norovirus capsid proteins from 1995 to 2006. *J. Virol.* **81**, 9932–9941 (2007).
- Koelle, K., Cobey, S., Grenfell, B. & Pascual, M. Epochal evolution shapes the phylodynamics of interpandemic influenza A (H3N2) in humans. *Science* **314**, 1898–1903 (2006).
- Lin, S. C. et al. Human norovirus exhibits strain-specific sensitivity to host interferon pathways in human intestinal enteroids. *Proc. Natl Acad. Sci. USA* **117**, 23782–23793 (2020).
- Alvarado, G. et al. Broadly cross-reactive human antibodies that inhibit genogroup I and II noroviruses. *Nat. Commun.* **12**, 4320 (2021).
- Ettayebi, K. et al. Replication of human noroviruses in stem cell-derived human enteroids. *Science* **353**, 1387–1393 (2016).
- Jiang, X., Wang, M., Graham, D. Y. & Estes, M. K. Expression, self-assembly, and antigenicity of the Norwalk virus capsid protein. *J. Virol.* **66**, 6527–6532 (1992).
- Ayyar, B. V. et al. CLIC and membrane wound repair pathways enable pandemic norovirus entry and infection. *Nat. Commun.* **14**, 1148 (2023).
- Conley, M. J. et al. Calicivirus VP2 forms a portal-like assembly following receptor engagement. *Nature* **565**, 377–381 (2019).

19. Chen, R., Neill, J. D., Estes, M. K. & Prasad, B. V. X-ray structure of a native calicivirus: structural insights into antigenic diversity and host specificity. *Proc. Natl Acad. Sci. USA* **103**, 8048–8053 (2006).
20. Williams, A. N. et al. Multiple signals in the gut contract the mouse norovirus capsid to block antibody binding while enhancing receptor affinity. *J. Virol.* **95**, e0147121 (2021).
21. Song, C. et al. Dynamic rotation of the protruding domain enhances the infectivity of norovirus. *PLoS Pathog.* **16**, e1008619 (2020).
22. Sherman, M. B. et al. Bile salts alter the mouse norovirus capsid conformation: possible implications for cell attachment and immune evasion. *J. Virol.* **93** <https://doi.org/10.1128/JVI.00970-19> (2019).
23. Jung, J. et al. High-resolution cryo-EM structures of outbreak strain human norovirus shells reveal size variations. *Proc. Natl Acad. Sci. USA* **116**, 12828–12832 (2019).
24. Devant, J. M., Hofhaus, G., Bhella, D. & Hansman, G. S. Heterologous expression of human norovirus GII.4 VP1 leads to assembly of T=4 virus-like particles. *Antivir. Res.* **168**, 175–182 (2019).
25. Devant, J. M. & Hansman, G. S. Structural heterogeneity of a human norovirus vaccine candidate. *Virology* **553**, 23–34 (2021).
26. Ossiboff, R. J., Zhou, Y., Lightfoot, P. J., Prasad, B. V. & Parker, J. S. Conformational changes in the capsid of a calicivirus upon interaction with its functional receptor. *J. Virol.* **84**, 5550–5564 (2010).
27. Wang, X. et al. Atomic model of rabbit hemorrhagic disease virus by cryo-electron microscopy and crystallography. *PLoS Pathog.* **9**, e1003132 (2013).
28. Hu, L. et al. Atomic structure of the predominant GII.4 human norovirus capsid reveals novel stability and plasticity. *Nat. Commun.* **13**, 1241 (2022).
29. Prasad, B. V. et al. X-ray crystallographic structure of the Norwalk virus capsid. *Science* **286**, 287–290 (1999).
30. Katpally, U., Wobus, C. E., Dryden, K., Virgin, H. W. T. & Smith, T. J. Structure of antibody-neutralized murine norovirus and unexpected differences from viruslike particles. *J. Virol.* **82**, 2079–2088 (2008).
31. Katpally, U. et al. High-resolution cryo-electron microscopy structures of murine norovirus 1 and rabbit hemorrhagic disease virus reveal marked flexibility in the receptor binding domains. *J. Virol.* **84**, 5836–5841 (2010).
32. Choi, J. M., Hutson, A. M., Estes, M. K. & Prasad, B. V. Atomic resolution structural characterization of recognition of histo-blood group antigens by Norwalk virus. *Proc. Natl. Acad. Sci. USA* **105**, 9175–9180 (2008).
33. Tan, M., Hegde, R. S. & Jiang, X. The P domain of norovirus capsid protein forms dimer and binds to histo-blood group antigen receptors. *J. Virol.* **78**, 6233–6242 (2004).
34. Lindesmith, L. C. et al. Sera antibody repertoire analyses reveal mechanisms of broad and pandemic strain neutralizing responses after human norovirus vaccination. *Immunity* **50**, 1530–1541 e1538 (2019).
35. Hansman, G. S. et al. Structural basis for broad detection of genogroup II noroviruses by a monoclonal antibody that binds to a site occluded in the viral particle. *J. Virol.* **86**, 3635–3646 (2012).
36. Shanker, S. et al. Structural basis for norovirus neutralization by an HBGA blocking human IgA antibody. *Proc. Natl Acad. Sci. USA* **113**, E5830–E5837 (2016).
37. Koromyslova, A. D. & Hansman, G. S. Nanobodies targeting norovirus capsid reveal functional epitopes and potential mechanisms of neutralization. *PLoS Pathog.* **13**, e1006636 (2017).
38. Koromyslova, A. D. & Hansman, G. S. Nanobody binding to a conserved epitope promotes norovirus particle disassembly. *J. Virol.* **89**, 2718–2730 (2015).
39. Kolawole, A. O. et al. Flexibility in surface-exposed loops in a virus capsid mediates escape from antibody neutralization. *J. Virol.* **88**, 4543–4557 (2014).
40. Williams, A. N. et al. A norovirus uses bile salts to escape antibody recognition while enhancing receptor binding. *J. Virol.* **95**, e0017621 (2021).
41. Ruoff, K. et al. Structural basis of nanobodies targeting the prototype norovirus. *J. Virol.* **93** <https://doi.org/10.1128/JVI.02005-18> (2019).
42. Koromyslova, A. D. et al. Nanobody-mediated neutralization reveals an Achilles heel for norovirus. *J. Virol.* **94** <https://doi.org/10.1128/JVI.00660-20> (2020).
43. Koromyslova, A. D., Morozov, V. A., Hefele, L. & Hansman, G. S. Human norovirus neutralized by a monoclonal antibody targeting the histo-blood group antigen pocket. *J. Virol.* **93** <https://doi.org/10.1128/JVI.02174-18> (2019).
44. Garaicoechea, L. et al. Llama nanoantibodies with therapeutic potential against human norovirus diarrhea. *PLoS One* **10**, e0133665 (2015).
45. Harmsen, M. M., van Solt, C. B., van Zijderveld-van Bommel, A. M., Niewold, T. A. & van Zijderveld, F. G. Selection and optimization of proteolytically stable llama single-domain antibody fragments for oral immunotherapy. *Appl. Microbiol. Biotechnol.* **72**, 544–551 (2006).
46. van der Vaart, J. M. et al. Reduction in morbidity of rotavirus induced diarrhoea in mice by yeast produced monovalent llama-derived antibody fragments. *Vaccine* **24**, 4130–4137 (2006).
47. Vuchelen, A. et al. (1)H, (13)C and (15)N assignments of a camelid nanobody directed against human alpha-synuclein. *Biomol. NMR Assign.* **3**, 231–233 (2009).
48. Tarr, A. W. et al. An alpaca nanobody inhibits hepatitis C virus entry and cell-to-cell transmission. *Hepatology* **58**, 932–939 (2013).
49. Mu, B. et al. Influenza virus detection with pentabody-activated nanoparticles. *J. Virol. Methods* **169**, 282–289 (2010).
50. Bobkov, V. et al. Nanobody-Fc constructs targeting chemokine receptor CXCR4 potently inhibit signaling and CXCR4-mediated HIV-entry and induce antibody effector functions. *Biochem. Pharm.* **158**, 413–424 (2018).
51. Strauss, M., Schotte, L., Thys, B., Filman, D. J. & Hogle, J. M. Five of five VHHs neutralizing poliovirus bind the receptor-binding site. *J. Virol.* **90**, 3496–3505 (2016).
52. Maffey, L., Vega, C. G., Mino, S., Garaicoechea, L. & Parreno, V. Anti-VP6 VHH: an experimental treatment for rotavirus a-associated disease. *PLoS One* **11**, e0162351 (2016).
53. Detalle, L. et al. Generation and characterization of ALX-0171, a potent novel therapeutic nanobody for the treatment of respiratory syncytial virus infection. *Antimicrob. Agents Chemother.* **60**, 6–13 (2016).
54. Alvarado, G. et al. Human monoclonal antibodies that neutralize pandemic GII.4 noroviruses. *Gastroenterology* **155**, 1898–1907 (2018).
55. Reeck, A. et al. Serological correlate of protection against norovirus-induced gastroenteritis. *J. Infect. Dis.* **202**, 1212–1218 (2010).
56. Bok, K. et al. Chimpanzees as an animal model for human norovirus infection and vaccine development. *Proc. Natl Acad. Sci. USA* **108**, 325–330 (2011).
57. Shanker, S. et al. Structural analysis of histo-blood group antigen binding specificity in a norovirus GII.4 epidemic variant: implications for epochal evolution. *J. Virol.* **85**, 8635–8645 (2011).
58. Haga, K. et al. Genetic manipulation of human intestinal enteroids demonstrates the necessity of a functional fucosyltransferase 2 gene for secretor-dependent human norovirus infection. *mBio* **11**, 2 (2020).
59. Ettayebi, K. et al. New insights and enhanced human norovirus cultivation in human intestinal enteroids. *mSphere* **6**, e01136-20 (2021).

60. Kou, B. et al. Characterization of cross-reactive norovirus-specific monoclonal antibodies. *Clin. Vaccin. Immunol.* **22**, 160–167 (2015).
61. Salmen, W. Positive and negative affinity chromatography to purify norovirus P-domain protein. *Methods Mol. Biol.* **2466**, 83–92 (2022).
62. Otwinowski, Z. & Minor, W. Processing of X-ray diffraction data collected in oscillation mode. *Methods Enzymol.* **276**, 307–326 (1997).
63. McCoy, A. J. et al. Phaser crystallographic software. *J. Appl. Crystallogr.* **40**, 658–674 (2007).
64. Liebschner, D. et al. Macromolecular structure determination using X-rays, neutrons and electrons: recent developments in Phenix. *Acta Crystallogr. D. Struct. Biol.* **75**, 861–877 (2019).
65. Emsley, P., Lohkamp, B., Scott, W. G. & Cowtan, K. Features and development of Coot. *Acta Crystallogr. D. Biol. Crystallogr.* **66**, 486–501 (2010).
66. Laskowski, R. A. & Swindells, M. B. LigPlot+: multiple ligand-protein interaction diagrams for drug discovery. *J. Chem. Inf. Model.* **51**, 2778–2786 (2011).
67. Pettersen, E. F. et al. UCSF Chimera—a visualization system for exploratory research and analysis. *J. Comput. Chem.* **25**, 1605–1612 (2004).
68. Schuck, P., Perugini, M. A., Gonzales, N. R., Howlett, G. J. & Schubert, D. Size-distribution analysis of proteins by analytical ultracentrifugation: strategies and application to model systems. *Biophys. J.* **82**, 1096–1111 (2002).
69. Laue, T. M., Shah, B., Ridgeway, T. M. and Pelletier, S. L. Computer-aided interpretation of analytical sedimentation data for proteins. 90–125. (Royal Society of Chemistry, 1992).
- nanobody. E.K. performed neutralization assays, W.S. expressed and purified the P-domain and crystallized it in complex with M4. W.S. L.H. and B.S. performed data collection and structure determination and analyzed the structure with B.V.V.P. W.S. and S.K. performed DLS and SV-AUC experiments, and A.V. performed endocytosis assay. F.H.N, R.L.A., and S.S. provided reagents. All authors reviewed, edited, and approved the final manuscript.

Competing interests

M.K.E. is named as an inventor on patents related to cloning of the Norwalk virus genome, is a consultant to Takeda Vaccines, Inc., and has received support from Takeda Vaccines, Inc. R.L.A. has received support from Takeda Vaccines, Inc. The remaining authors declare no competing interests.

Additional information

Supplementary information The online version contains supplementary material available at <https://doi.org/10.1038/s41467-023-42146-0>.

Correspondence and requests for materials should be addressed to B. V. Venkataram Prasad.

Peer review information *Nature Communications* thanks Mihnea Bostina and the other, anonymous, reviewer(s) for their contribution to the peer review of this work. A peer review file is available.

Reprints and permissions information is available at <http://www.nature.com/reprints>

Publisher's note Springer Nature remains neutral with regard to jurisdictional claims in published maps and institutional affiliations.

Open Access This article is licensed under a Creative Commons Attribution 4.0 International License, which permits use, sharing, adaptation, distribution and reproduction in any medium or format, as long as you give appropriate credit to the original author(s) and the source, provide a link to the Creative Commons licence, and indicate if changes were made. The images or other third party material in this article are included in the article's Creative Commons licence, unless indicated otherwise in a credit line to the material. If material is not included in the article's Creative Commons licence and your intended use is not permitted by statutory regulation or exceeds the permitted use, you will need to obtain permission directly from the copyright holder. To view a copy of this licence, visit <http://creativecommons.org/licenses/by/4.0/>.

© The Author(s) 2023

Acknowledgements

We acknowledge the Advanced Light Source (8.2.2) (Berkeley, CA) for X-ray data collection. The ALS-ENABLE beamlines are supported in part by the National Institutes of Health, National Institute of General Medical Sciences, grant P30 GM124169-01. The Advanced Light Source is a Department of Energy Office of Science User Facility under Contract No. DE-AC02-05CH11231. This work was supported by N.I.H. grant P01 AI057788 (to M.K.E, R.L.A, and B.V.V.P.) and a grant from the Robert Welch Foundation (to B.V.V.P.). P30 CA125123 supported the Protein and Monoclonal Antibody Production Shared Resource at Baylor College of Medicine for VLP expression and SV-AUC. We also thank Fulbright Program for a grant for Dr. Bok to travel to NIH for HIE experiments. This work was also supported, in part, by the Division of Intramural Research, NIAID, NIH.

Author contributions

W.S., L.H., B.V.V.P., and M.K.E. conceived and designed the research in collaboration with V.P., M.B., E.K., S.V.S., and K.G. who provided the M4